Understanding three-dimensional effects in polarized observations with the ground-based ADMIRARI radiometer during the CHUVA campaign

Understanding three-dimensional effects in polarized observations with the ground-based ADMIRARI radiometer during the CHUVA campaign

Alessandro Battaglia,[1] Pablo Saavedra,[2] Carlos Augusto Morales,[3] and Clemens Simmer[2]

Received 15 November 2010; revised 11 February 2011; accepted 17 February 2011; published 10 May 2011.

[1] Measurements of down-welling microwave radiation from raining clouds performed with the Advanced Microwave Radiometer for Rain Identification (ADMIRARI) radiometer at 10.7–21–36.5 GHz during the Global Precipitation Measurement Ground Validation "Cloud processes of the main precipitation systems in Brazil: A contribution to cloud resolving modeling and to the Global Precipitation Measurement" (CHUVA) campaign held in Brazil in March 2010 represent a unique test bed for understanding three-dimensional (3D) effects in microwave radiative transfer processes. While the necessity of accounting for geometric effects is trivial given the slant observation geometry (ADMIRARI was pointing at a fixed 30° elevation angle), the polarization signal (i.e., the difference between the vertical and horizontal brightness temperatures) shows ubiquitousness of positive values both at 21.0 and 36.5 GHz in coincidence with high brightness temperatures. This signature is a genuine and unique microwave signature of radiation side leakage which cannot be explained in a 1D radiative transfer frame but necessitates the inclusion of three-dimensional scattering effects. We demonstrate these effects and interdependencies by analyzing two campaign case studies and by exploiting a sophisticated 3D radiative transfer suited for dichroic media like precipitating clouds.

Citation: Battaglia, A., P. Saavedra, C. A. Morales, and C. Simmer (2011), Understanding three-dimensional effects in polarized observations with the ground-based ADMIRARI radiometer during the CHUVA campaign, *J. Geophys. Res.*, *116*, D09204, doi:10.1029/2010JD015335.

1. Introduction

[2] Although three-dimensional (3D) radiative transfer (RT) effects within cloudy atmospheres have been theoretically quantified via sophisticated radiative transfer tools [e.g., *Marshak and Davis*, 2005], their observation has been always extremely elusive. The main reason is the enormous difficulty to perform closure studies with a full characterization of the radiatively important 3D structure of a cloud. Hence observational studies toward 3D effects have been statistical in nature, for example, by analyzing satellite measurements in ways that illustrate dependencies that are inconsistent with the assumption of 1D RT. Emphasis has always been put on shortwave solar radiances particularly for the understanding of the relationship between cloud albedo, cloud microphysics and cloud structure, which is of great interest for studies of equilibrium climate and climate change. This research avenue has been boosted by the rising number of satellites with increasingly higher spectral and spatial resolution and more viewing angles (e.g., the Aerosol Polarimetric Sensor on board the upcoming GLORY mission [*Mishchenko et al.*, 2007]).

[3] In this paper, we focus on 3D RT in the microwave region with a specific interest in precipitation, which is known to have a high spatiotemporal heterogeneity. The latter represents a caveat for all microwave-based remote sensing techniques; already in the late 1970s, *Weinman and Davies* [1978] used both analytical and Monte Carlo 3D RT models to quantify the so-called nonuniform beam filling (NUBF) effect in passive microwave retrievals of rain rate. The beam-filling effect arises from the assumption of homogeneous rainfall across the field of view (FOV), coupled with the nonlinear, concave-downward response of brightness temperatures (T_Bs) to rainfall rate. The effect depends mainly on the footprint dimension, the microwave frequency under investigation, the cloud type and shape, and in all cases increases with inhomogeneity and mean LWP or rain rate [*Kummerow*, 1998; *Lafont and Guillimet*, 2004]. NUBF was found to be the main source of error in retrieved rainfall rate from spaceborne microwave radiometers; an uncertainty of a factor of 2 can exist in the mean rain rate for a given brightness temperature [*Weinman and Davies*, 1978; *Lafont and Guillimet*, 2004].

[4] The presence of inhomogeneity in the instrument FOV, and more generally the 3D structure of the system

[1]Department of Physics and Astronomy, University of Leicester, Leicester, United Kingdom.
[2]Meteorological Institute, University of Bonn, Bonn, Germany.
[3]Instituto de Astronomia, Geofisica e Ciéncias Atmosféricas, Universidade de São Paulo, São Paulo, Brazil.

0148-0227/11/2010JD015335

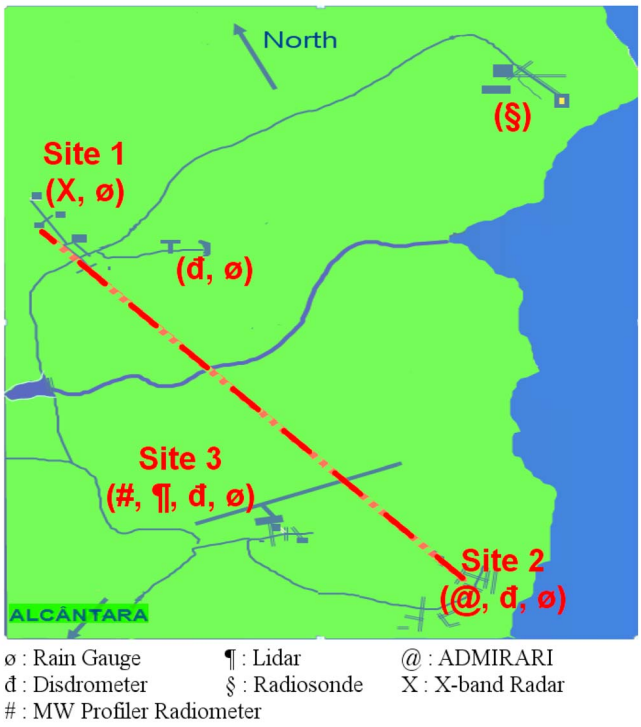

Figure 1. Site scheme for the CHUVA campaign with the location of all the instruments. The dash-dotted line indicates the direction of observation for ADMIRARI (Site 2) and of the RHI scans of the X band radar (Site 1). The distance between sites 1 and 2 is 7.65 km.

under observation, does not preclude the use of 1D radiative transfer approaches. In fact the plane-parallel assumption does not require homogeneity at distances arbitrarily far from the FOV of the sensing instrument. For instance, for pure absorbing atmospheres and Fresnel-like surfaces, the radiation sensed by spaceborne passive microwave radiometers originates exclusively from the FOV projected slant tube. In these cases, 1D independent pixel approximations work very well, with the simple expedient of taking into account geometric effects in case of off-nadir looking radiometers [*Battaglia et al.*, 2005]. In the slant path (SP) approximation [*Bauer et al.*, 1998; *Roberti et al.*, 1994] the structure is horizontally homogeneous while the vertical profile is reconstructed by using the slant profile defined by the ray traced from the sensor upward to the TOA for ground-based or downward to the surface and then reflected upward for spaceborne radiometers.

[5] In the presence of scattering media and/or diffusive surfaces, due to the redirecting of radiation by diffusion events, radiation sensed by the radiometer may not be generated within the slant tube of observation. In this case the horizontal displacement of radiation in directions perpendicular to the viewing direction produces scattering effects, which are more subtle and difficult to treat. The study of these effects has matured with the simultaneous development of 3D RT codes, mainly based on Monte Carlo techniques [*Roberti et al.*, 1994; *Liu et al.*, 1996; *Roberti and Kummerow*, 1999].

[6] *Kummerow* [1998] and *Roberti and Kummerow* [1999] noticed that, compared to the correct 3D simulations, the 1D SP modeling introduces mainly random errors and only minor bias errors. In fact, in 1D SP approximations, radiation remains trapped by construction in the slant tube: no contribution from outside the tube is allowed, possibly resulting in nonphysical variations for contiguous pixels. A 3D radiation field can be depicted as a smoothed version of the field constructed from many 1D radiation simulations. The computed $\Delta T_B = T_B\,[3D] - T_B\,([1DSP]$ leads to large differences (>10 K) for TRMM Microwave Imager resolutions only at the highest frequency (85.5 GHz, 5 km resolution). Areas with positive ΔT_B are generally followed immediately by areas with negative ΔT_B, thus confirming the overall cancelation of the bias.

[7] Only recently, attention has turned toward studies involving 3D effects in the polarization signal. This has been fostered by the introduction of full polarimetry in Monte Carlo RT codes [*Battaglia and Mantovani*, 2005; *Davis et al.*, 2005; *Battaglia et al.*, 2007], which are now capable of treating dichroic media. While spherical particles are known to produce small polarization signals at microwave frequencies [*Liu and Simmer*, 1996], preferentially oriented nonspherical particles are potentially more effective in that respect. Two main scenarios have been studied so far.

[8] 1. *Davis et al.* [2007] accurately simulated observations of 3D midlatitude preferentially oriented cirrus clouds (synthetically generated from 2D observations of the Chilbolton radar at a resolution of approximately 780 m by 780 m by 110 m) for a variety of viewing geometries corresponding to operational (Advanced Microwave Sounding Unit AMSU-B, Earth Observing System–Microwave Limb Sounder EOS-MLS) and proposed (Cloud Ice Water Sub-millimetre Imaging Radiometer CIWSIR) high-frequency spaceborne radiometers. For the AMSU-B 190.3 GHz and the CIWSIR 334.65 and 664 GHz channels, they demonstrated the significance of polarization effects for nonspherical particles, and also of beam-filling effects with regard both to intensity and to polarization. They found a good agreement between 3D and the independent pixel approximation (IPA), which suggests that for slant viewing instruments (with footprint radii of 5.5 km (CIWSIR) or 16 km (AMSU-B)) and low tangent height limb sounding, 3D scattering RT effects do not have a significant impact and show unequivocal signatures as well. Their study is purely notional; no (statistical) analysis with observations has been performed.

[9] 2. *Battaglia et al.* [2006] studied 3D RT effects in ground-based low microwave frequency (10–36 GHz) radiometric observations of rain. As theoretically proposed by *Czekala and Simmer* [1998] and confirmed by *Czekala et al.* [2001a], larger drops exhibit negative polarization differences ($PD \equiv T_B^V - T_B^H$) in the downwelling microwave radiation which can be exploited in discriminating between cloud and rain liquid water [*Czekala et al.*, 2001b]. The basis for this information is the assumption of a well-defined equilibrium shape of raindrops and their orientation distribution in absence of turbulence and wind shear [e.g., *Andsager et al.*, 1999]. *Battaglia et al.* [2006] demonstrated that 3D effects tend to modify the distribution of observations in the $T_B - PD$ plane, which exhibits a parabolic shape

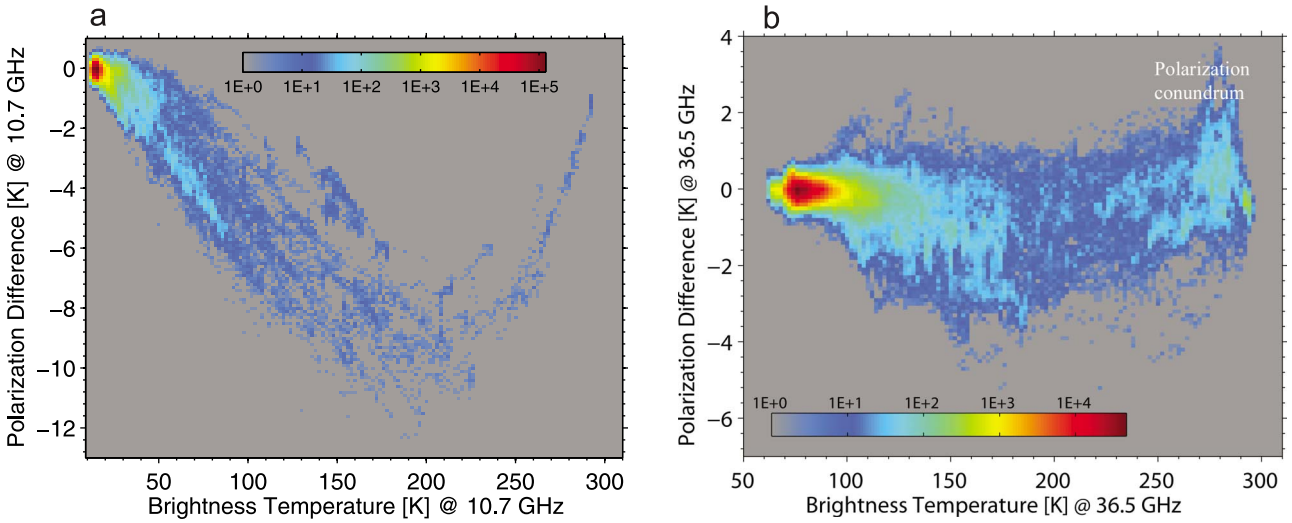

Figure 2. ADMIRARI measurements collected during the CHUVA campaign displayed in the $T_B - PD$ plane at (a) 10.7 and (b) 36.5 GHz. The colorbar indicates the number of occurrences on a logarithmic scale.

with a negative *PD* minimum at intermediate T_Bs (e.g., see Figures 2 and 3 of *Czekala et al.* [2001a] or Figure 4 of *Battaglia et al.* [2010]). The 3D effects may alter the amplitude of the minimum *PD* and the general slope in the ascending and descending part of the curve. More subtle effects like nonzero *PD*s at nadir and also nonzero third Stokes vector components may occur. *Battaglia et al.* [2006] concluded that a 1D SP approximation is generally insufficient for scenarios with high rain rates; here the *PD* signal is the most affected.

[10] To further advance this second research avenue, Advanced Microwave Radiometer for Rain Identification (ADMIRARI) was developed and deployed in different field campaigns [*Battaglia et al.*, 2009, 2010]. A Bayesian scheme including 3D RT simulations designed for the ADMIRARI suite of measurements retrieves simultaneously water vapor, rain and cloud liquid water paths for the slant volume under observation.

[11] The goal of this study is to deepen our understanding of 3D RT effects in passive low-frequency and polarized ground-based observations of microwaves signal. In particular we aim at validating the conjectures and predictions proposed by notional RT studies with field measurements. Thanks to their proximity to the target which results in narrow FOV, ground-based radiometry has a huge potential in that respect because polarization features produced by 3D structures can be observed without having to contend with NUBF effects, which tend to smooth them out. The March 2010 Global Precipitation Measurement Ground Validation "Cloud processes of the main precipitation systems in Brazil: A contribution to cloud resolving modeling and to the Global Precipitation Measurement" (CHUVA) campaign represents a perfect test bed given the distinct structures of the observed typical precipitating systems and the measurement setup (section 2). Two situations are investigated in detail (section 3), which provides excellent examples of pristine 3D RT effects (section 4). Unique scattering 3D RT features are identified in the observations and explained by comparing 3D backward Monte Carlo and 1D SP RT simulations (section 5). Conclusions are drawn in section 6.

2. The CHUVA Field Campaign

[12] As part of CHUVA, several field campaigns will take place in Brazil (during 2010–2013) to support the Brazilian activities of the GPM-Brazil program toward the cooperation between the Brazilian Space Agency-AEB and NASA Ground Validation program (GPM/GV). The first campaign, PRE-CHUVA took place at the Brazilian Launching Center of Alcăntara (CLA) in northeastern Brazil from 1 to 25 March 2010 (http://gpmchuva.cptec.inpe.br). According to CHUVA objectives, in this field experiment the measurements were concentrated to depict the warm rain process and their transition to the vertically developed tropical precipitating systems. During the campaign, AEB, the Brazilian Air Force at CLA, the Space Research Institute (INPE), University of São Paulo, University of Bonn and NASA provided several instruments to support the PRE-CHUVA campaign. Figure 1 provides the location of the sensors deployed for this field experiment: X Doppler Dual Polarization weather radar, automatic weather stations, radiosondes, disdrometers (JOSS, Parsivel and Thiess), rain gauges, lidar, the Radiometrics MP3000 Microwave Radiometer and the ADMIRARI radiometer. For the present study, we focus on measurements taken only by ADMIRARI and the X band weather radar.

[13] As depicted in Figure 1, ADMIRARI was located at the Delta village (latitude 2°23.16′S, longitude 44°22.8′W, Site 2) and it was aligned at southeast of the weather radar (latitude 2°19.5′S, longitude 44°25.2′W, site 1) at 7.65 km. Along this radial, several ancillary observations were taken in the airport (latitude 2°22.6′S, longitude 44°24′W, site 3). For the campaign, the radar strategy was repeated every 10 min and it was composed of one volume scan with 12

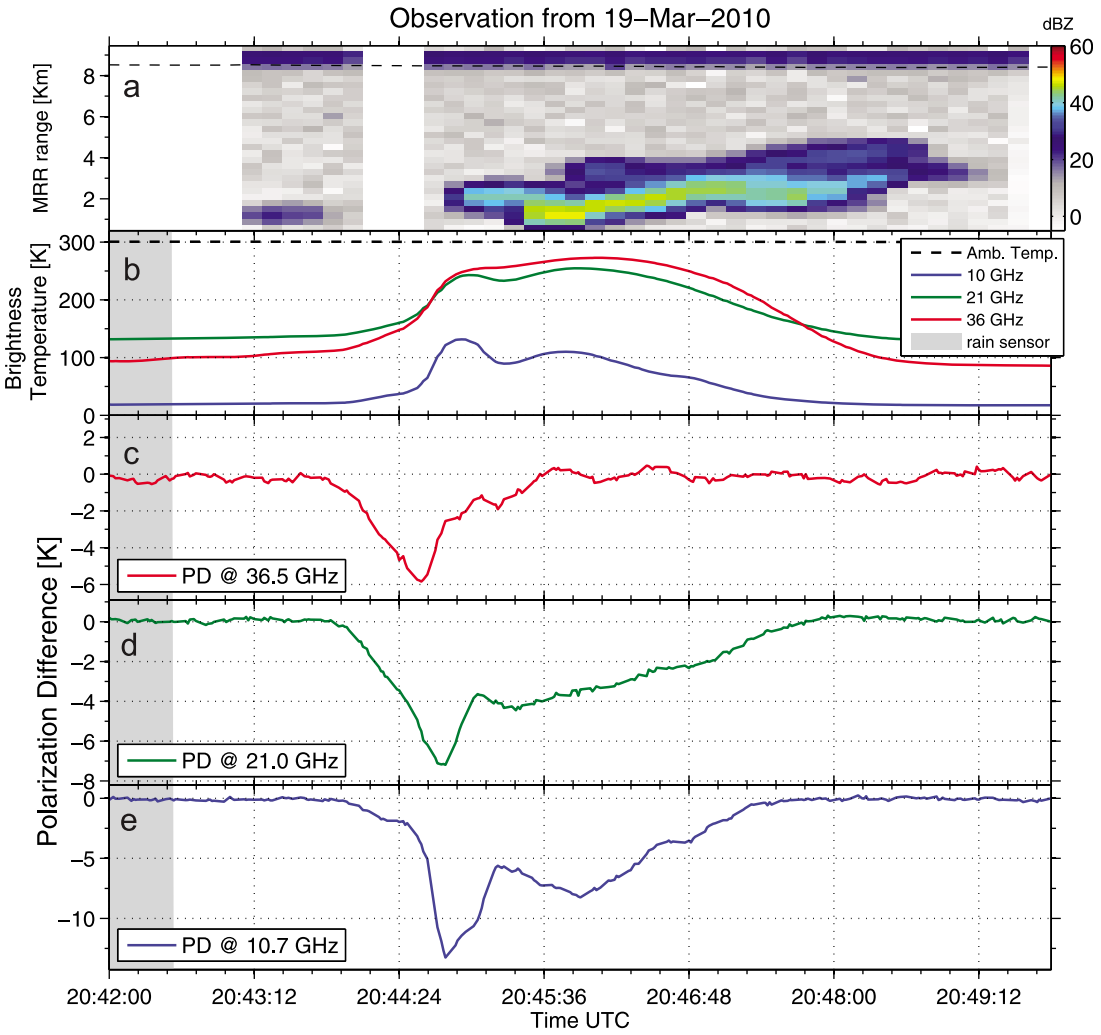

Figure 3. Measurements from 19 March 2010 at 30° elevation angle. (a) MRR reflectivity in dBZ. The dashed line corresponds to the range location of the freezing level as identified by the closest radiosounding. (b) Brightness temperature for the three frequencies. Polarization difference at (c) 36, (d) 21, and (e) 10 GHz. Gray areas indicate rainy periods flagged by the rain sensor collocated with ADMIRARI.

elevations and one range height indicator (RHI) along the ADMIRARI direction. The volume scans were set to start at 00, 10, 20, 30, 40 and 50 min every hour, while the RHI was at 06, 16, 26, 36, 46, 56 min. The radar was set to collect radar reflectivity (Z), Doppler velocity and spectral width, differential reflectivity (Z_{DR}), differential phase (Φ_{DP}) and correlation between horizontal and vertical polarization (ρ_{HV}) with gate width of 125 m. The RHI scan strategy varied from 0 to 90° every 0.5° elevation steps. ADMIRARI was set to observe at a constant 30° elevation angle in the direction toward the weather radar, Site 1. ADMIRARI measurements comprise T_Bs at vertical and horizontal polarization at its three frequencies (10.7–21.0–36.5 GHz); the T_Bs were complemented by slant reflectivity profiles observed at 24.1 GHz by a Micro Rain Radar (MRR) [see, e.g., *Peters et al.*, 2002] at 30° elevation angle with 300 m range resolution and 31 bins. In addition, rain occurrence over the radiometer position from a rain sensor, ambient temperature and pressure as well as internal receiver and stability temperatures were recorded for quality control.

[14] During the Pre-CHUVA, three marked weather regimes could be found based on the radar and gauge measurements: (1) during the first two weeks, dry weather conditions without significant precipitation prevailed; (2) in the third week, isolated and short warm rain cells were observed; and (3) finally, the last week was marked by the rainiest period that included several warm rain events and deep convective storms with a wide range of intensity and duration. As most of these raining systems are small and convective, a large variability on the rain gauge and disdrometer accumulation was found at the three sites, i.e., 250 mm, 200 mm and 270 mm rain accumulation for 13, 9 and 9 days at site 1 (Radar), site 2 (ADMIRARI) and site 3 (CLA), respectively.

[15] Figure 2 summarizes all ADMIRARI measurements collected during the CHUVA campaign in the $T_B - PD$ plane. Two features are striking: in Figure 2a, extremely large T_Bs at 10.7 GHz hint at extreme events with high optical thicknesses characteristic for tropical regions (including an unique event reaching saturation level in the radiometric signal, a feature observed at this frequency for the first time);

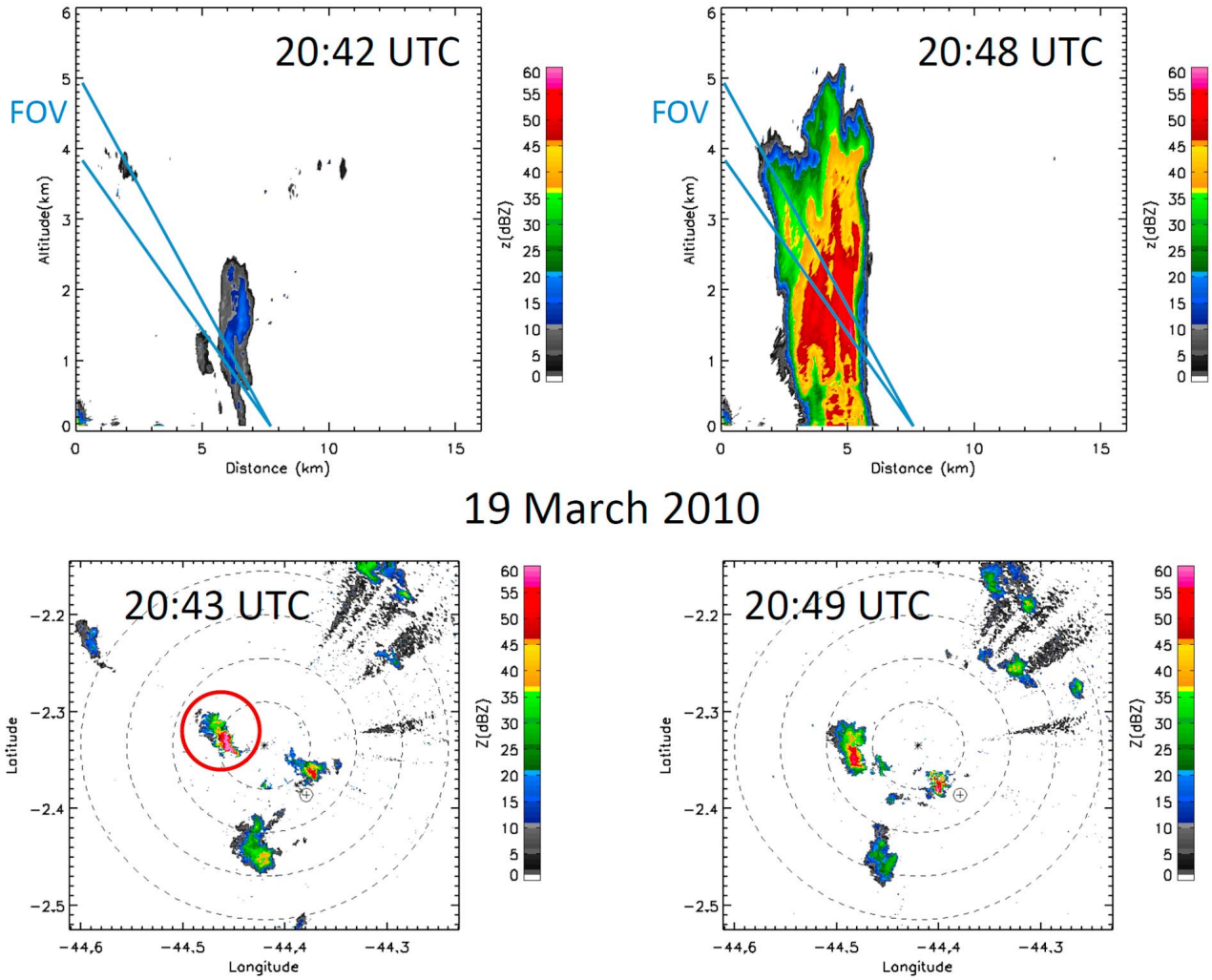

Figure 4. Radar (top) range height indicator (RHI) and (bottom) plane position indicator (PPI) sequence for the event of 19 March 2010. The RHI scans are performed every 6 min toward ADMIRARI. ADMIRARI position (FOV) is indicated by a cross (cone) in the PPI (RHI) plots. The radiometer is located 7.65 km away from radar.

and in Figure 2b, in the region with T_Bs close to saturation (i.e., close to ambient temperature) positive *PD*s are ubiquitous both at 36.5 (shown) and at 21.0 GHz (not shown). These features will be discussed in detail in sections 3 and 4.

3. Case Studies

3.1. Scenario from 19 March

[16] The first case analyzed is a 6 min long rain shower, which occurred on 19 March 2010 around 2045 UTC. The ADMIRARI observations (i.e., MRR slant reflectivity profiles, T_Bs and *PD*s at 10–21–36 GHz) are depicted in Figure 3. This case represents typical situations encountered during the campaign: rain-bearing cells were forming over the ocean, were advected inland, and passed ADMIRARI. ADMIRARI was looking roughly orthogonal to the flow direction, with the rain cells coming from the northeast toward the southwest (i.e., roughly following the same line as the airport pad in Figure 1). The MRR slant reflectivity profiles clearly identify that this particular event was observed mostly with the radiometer being outside the rain cell; this is corroborated by the rain sensor (gray area in Figures 3 and 6) which did not flag rain during the period under consideration. This evolution is also confirmed by the series in the RHIs (Figure 4). Note that the rain shaft is not very deep along the line of sight of the radiometer, which partially explains why only the highest frequency is reaching complete saturation, and only for a very short period. Compared to the MRR profiles, the onset of precipitation appears to be anticipated in the ADMIRARI measurements, with all *PD*s being negative from 2043:54 UTC onward. Looking at the plane position indicator (PPI) radar image (Figure 4, bottom), this seems to be caused by a more distant rain cell (beyond the MRR ranging distance) which was passing earlier through the ADMIRARI line of sight (circled in red in Figure 4, bottom left).

[17] The time evolution of the ADMIRARI observed variables in the $T_B - PD$ plane (Figure 5) showcases a recurrent pattern during the CHUVA campaign. Apart from variations which can be related to the time evolution of the

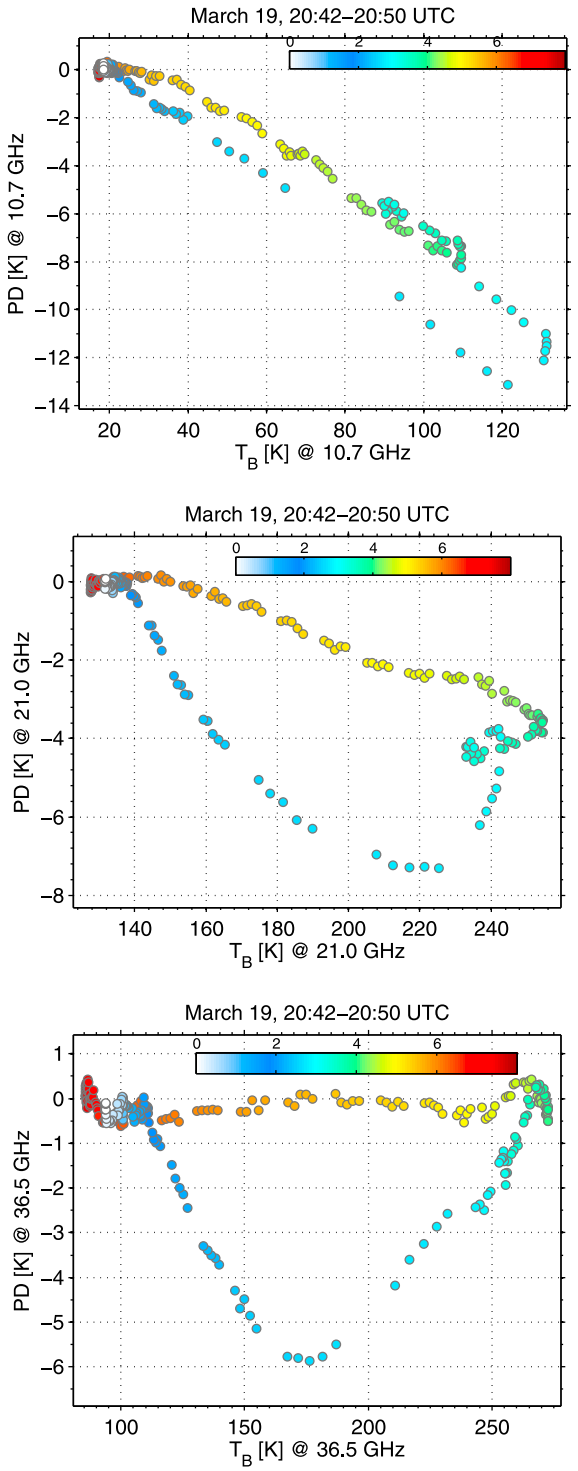

Figure 5. Event of 19 March 2010: time evolution in the $T_B - PD$ plane for the three ADMIRARI frequencies. The overall duration of the event is 8 min. The colorbar modulates the time passed in minutes from the beginning of the event at 2042 UTC.

system itself, the 10 GHz time series is as expected: in the beginning both the T_B (the absolute *PD*) values gradually increase with the rain cell entering the *FOV* up to 125 (13) K and then gradually decrease when the rain cell exits the *FOV*. Note that on the exit path, *PD*s with similar T_Bs as during the entering path are characterized by lower absolute values; this is most probably caused by the fact that the ADMIRARI *FOV* is intercepting an increasing cloud component (e.g., compare the *FOV*s in Figure 13) which reduces the *PD*s, because of the spherical shapes of cloud droplets. The 36.5 GHz pattern is completely different, with T_B reaching the highest values of 265 K (still 35 K below the ambient temperature of 27°C) after passing a minimum *PD* of −6 K around 170 K. From saturation on, the T_Bs go back to the clear-sky value at 85 K with *PD*s straddling around 0 K. The 21 GHz observations have an intermediate behavior.

[18] The observed 36.5 GHz signal evolution is totally unexpected in a pure 1D world: all the observation pairs from 2045 UTC onward do not fit Figure 3 of *Czekala* [1998] or Figure 4 of *Battaglia et al.* [2010], which are both based on 1D simulations without slant path approximations. The series of 36.5 GHz observations with decreasing T_Bs and zero *PD*s would be associated with a profile only containing cloud droplets, with lower and lower contents with time. But this is obviously not the case because the 10 GHz signal shows significant negative *PD*s, and the MRR observed reflectivities are well above the noise level (due to their low signal cloud droplets are well below the noise level of such an instrument). The fact that all our observations are performed at 30° introduced significant geometric effects, but this will only partially explain the observed feature for this instance.

3.2. Scenario From 20 March

[19] The observations from 20 March indicate an extreme scenario with a first period of observation made from outside the rain cell (until 1007 UTC) and then from inside the rain cell as depicted by the rain sensor in Figure 6. The convective cells under observation were much more intense and larger than those from the previous day as clearly shown by the RHI radar observations (Figure 7); the event also lasted much longer (around 45 min). For most of the time the 21.0 and 36.5 GHz T_Bs were fully saturated (around 18 min saturation), even the 10 GHz T_Bs reached extraordinary high values up to 280 K (see Figure 6). At certain instants also the MRR signal is fully attenuated by the rain cell. A 21 GHz T_B around 180 (250) K corresponds approximately to a slant optical thickness of 1 (2); assuming the same for the 24.1 GHz MRR frequency, this corresponds to a 8.5 (17) dB two-way attenuation. Therefore for instants when the 21 GHz T_Bs exceed 250 K the MRR backscattering signal coming from the more distant precipitating volume will be most likely lost.

[20] The time evolution of the event in the $PD - T_B$ plane (Figure 8) shows a remarkable variability of the *PD*s at saturated T_Bs both at 21.0 and 36.5 GHz with positive polarization values up to +4 K and +2.1 K, respectively. As discussed hereafter, these features represent a conundrum which can only be explained via 3D RT.

4. The 3D Polarized Simulations of Precipitating Clouds

[21] To understand some of the features observed by ADMIRARI during CHUVA, we resort to a very simple box cloud scenario following ideas similar to *Battaglia et al.*'s [2006] (see Figure 9). To resemble the situation

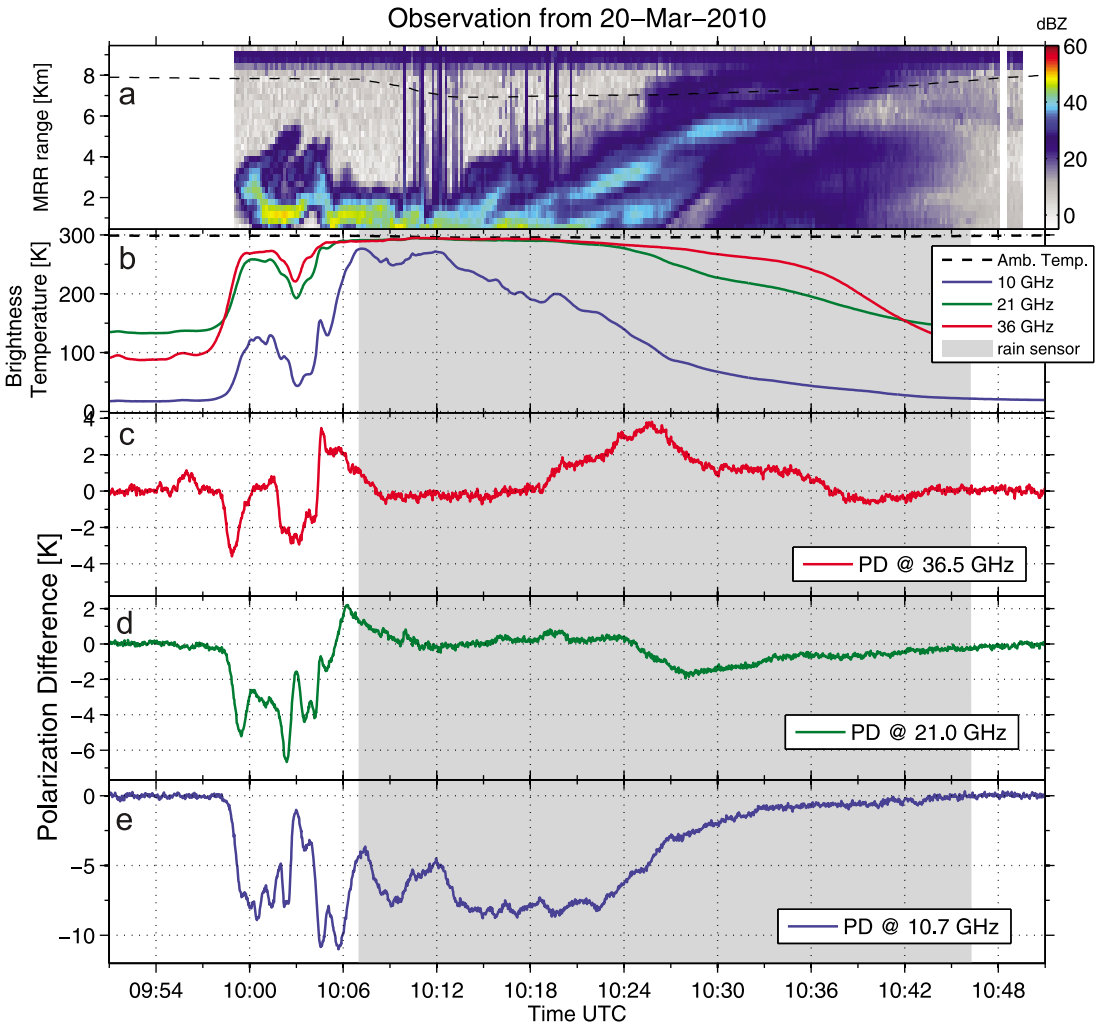

Figure 6. Measurements from 20 March 2010 at 30° elevation angle. (a) MRR reflectivity in dBZ (color scale coded). (b) Brightness temperature for the three frequencies. Polarization difference at (c) 36, (d) 21, and (e) 10 GHz. Gray areas indicate rainy periods flagged by the rain sensor.

encountered on 20 March 2010, a $L_{cx} \times L_{al} = 4 \times 4 = 16$ km^2 box with liquid water paths of 20.0 and 3.6 kg/m^2 of the rain and cloud component, respectively, was assumed with a cloud base located around 2.5 km and a rain column reaching up to 4 km (similar to that shown later on in Figure 15 (top left). This profile matches the radar observations around 1006 UTC (Figure 7, top middle). Note that later on the cell developed some hail as evident from the presence of flare echoes at 1024 and 1030 UTC.

[22] In the lowest levels with rain content of the order of 3 g/m^3 (corresponding to 13.8 kg/m^2 in the slant path), the extinction coefficients are around 0.5, 2 and 5 km^{-1} for the three ADMIRARI frequencies, with single scattering albedos ranging from 0.36 to 0.53. T_Bs and PDs are simulated (Figure 10, only 10.7 and 36.5 GHz) as sensed by an ADMIRARI-like radiometer (i.e., with a 3dB beam width of 6.5°) located at different positions inside and outside the rain shaft with an elevation angle of 30°. The color coding in Figure 10 quantifies the simulated measurements looking "southward," i.e., along the negative y axis. In the following the position of the radiometer will be identified by two coordinates: a cross- and an along-ground projected line-of-sight (GP-LOS) distance. In such a reference frame the rain shaft is indicated by the thick black rectangle with corners located at (0,0),(0,4),(−4,4),(−4 km,0 km) in Figure 10 (bottom left); because of the symmetry of the problem all plots are cut at a cross-LOS distance equal 2 km, i.e., in the middle of the cloud.

[23] There are obviously border/edge effects due to the finite antenna beam width of the radiometer, which causes the spill-out of rain shaft–generated radiation in the region with negative cross-GP-LOS distances as well. The effect is roughly restricted to the conical area identified by the dashed thick black lines in Figure 10 (bottom left), with the conical vertex angle being half the radiometer 3dB beam width. For observation points within such areas, the observed volume will be nonuniformly filled. An extreme scenario is achieved when half of the beam is filled by the rain shaft and half by clear sky (cross-GP-LOS distance equal to 0 km). If the radiometer is located to the north of the rain shaft and looking toward the shaft at an along-GP-LOS distance of around 4 km, the region affected by NUBF is about 0.75 km wide. This corresponds roughly to 3 min for a precipitation cell moving at 20 km/h in the direction orthogonal to the

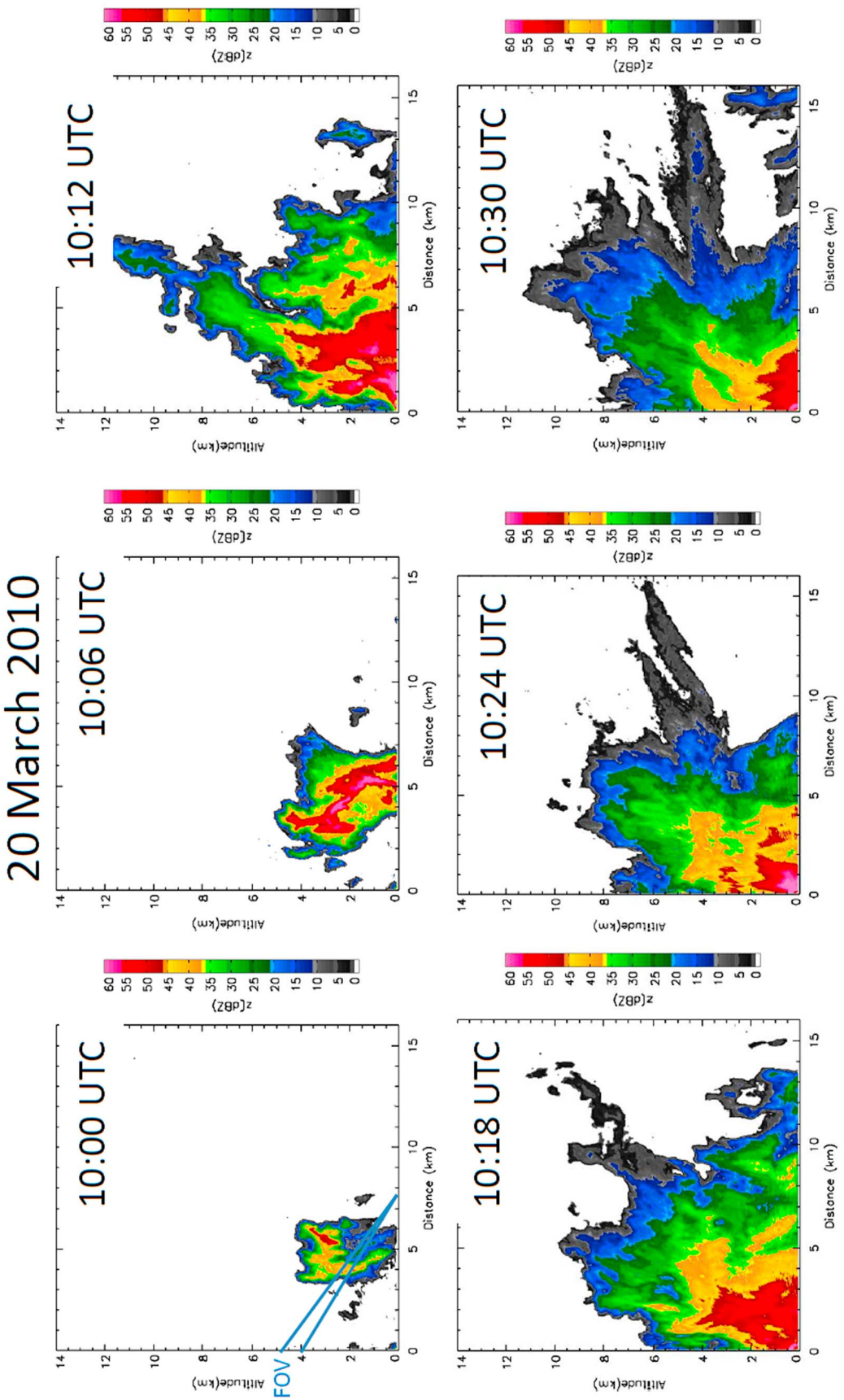

Figure 7. Radar RHI sequence for the event of 20 March 2010. The RHI scans are performed every 6 min toward ADMIRARI. The ADMIRARI FOV is indicated by the blue cone in the top left panel.

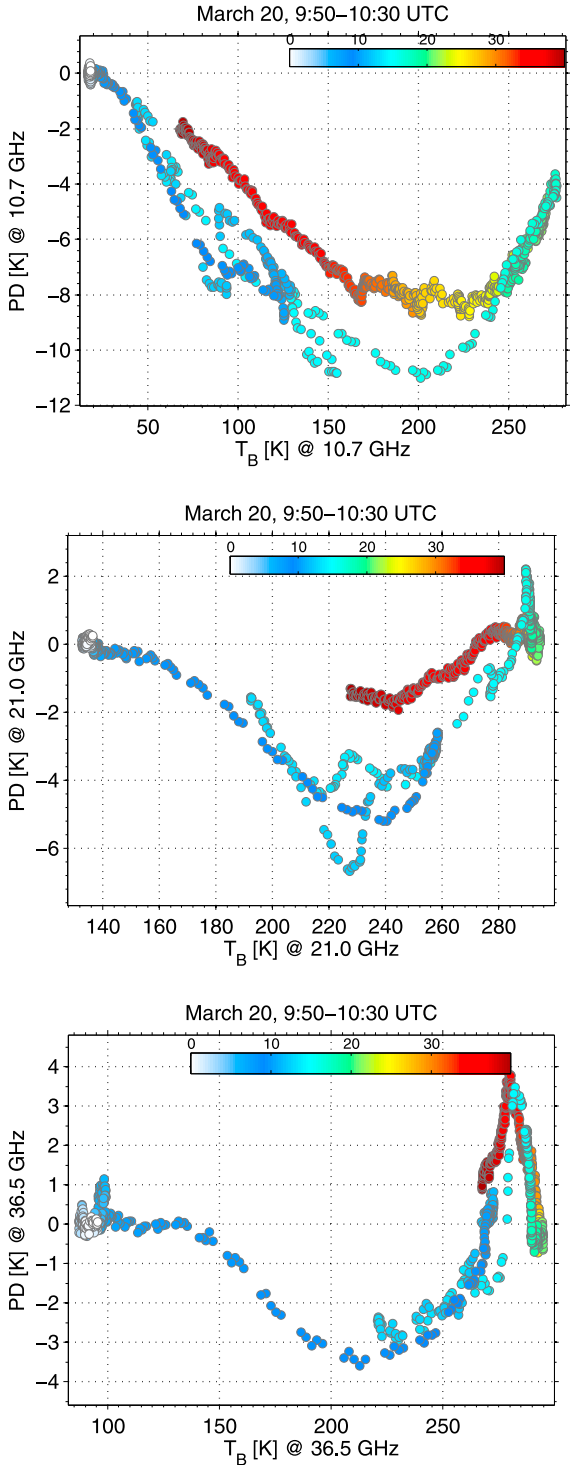

Figure 8. Event of 20 March 2010: time evolution in the $T_B - PD$ plane for the three ADMIRARI frequencies. The overall duration of the event is 40 min. The colorbar modulates the time passed in minutes from the beginning of the event at 0950 UTC.

radiometer viewing direction. In the NUBF-affected region the radiation field is clearly characterized by a strong gradient. Certainly the situation is extreme due to the unrealistic sharp edge of the rain shaft assumed, but it is indicative of an important pitfall of the measurements, as we see later.

[24] To have a deeper understanding of the RT, we restrict our analysis to a cross-GP-LOS distance equal to 2 km along the double array dash-dotted line depicted in Figure 10 (bottom left). Thus ADMIRARI "looks" toward the center of the rain shaft, and we vary the distance from the rain shaft (Figure 11). With this selection we avoid the NUBF affected area so that "lateral" NUBF effects do not play any role for these radiometer viewing positions. The continuous lines in Figure 11 indicate the ADMIRARI T_B and *PD*s including all scattering order contributions via a full 3D simulation (backward Monte Carlo [*Battaglia et al.*, 2007]). The black diamond line shows the corresponding measurements simulated for a radiometer with a pencil beam via a full 3D simulation (backward Monte Carlo [*Battaglia et al.*, 2007]). Thus we can study resolution effects. The dashed red line provides also the results for a radiometer with a pencil beam but obtained from a slant path 1D simulation (adapted RT4 code [*Evans and Stephens*, 1991]). We can draw the following observations.

[25] 1. At 36.5 GHz (10.7 GHz), in the region with the highest T_Bs, half (10%) the total radiation has encountered at least one scattering event (see the difference between black continuous and red diamond lines in Figure 11 (left)). Therefore at the higher frequencies the scattered field is expected to largely affect the radiometer signal; thus 3D scattering effects are likely to occur.

[26] 2. The emission (i.e., zero order of scattering) term is very different at the three frequencies because of the different downwelling atmospheric emission (see equations (1) and (2) of *Battaglia et al.* [2006] for details). $PD^{[0]}$ (diamond red lines in Figure 11, right) is the result of two processes: (1) the propagation of radiation in rain that is vertically polarizing due to the increased absorption of horizontally polarized radiation and (2) the emission of radiation, which is preferentially horizontally polarized. At 21 and 36.5 GHz, due to the presence of a considerable background emission from behind the rain shaft, the propagation effect tends to overcome the emission resulting in positive $PD^{[0]}$ s for all optical thicknesses. Conversely, at 10 GHz, this happens only for large optical thicknesses, while for thin media, $PD^{[0]}$ is negative.

[27] 3. The impact of the higher orders of scattering on *PD*s is much larger than the impact on T_Bs. For instance, at 10 GHz, the *PD*s may be affected for more than 50% by the radiation scattered within the observed volume (Figure 11, top right; compare red diamond and black continuous lines).

[28] 4. The total signal simulated for an ADMIRARI 3dB beam width (6.5 degrees) significantly differs from the pencil beam only when the along-GP-LOS distance from the rain shaft exceeds 4 km (compare the black continuous and diamond black dash-dotted lines in Figure 11, right). This is due to the NUBF which is responding to the vertical variability of the precipitating cloud. The overall effect is equivalent to spatially smoothing out the *PD* and T_B fields obtained in the pencil beam configuration along the viewing direction.

[29] 5. In all situations the 1D pencil beam shows smaller (larger) T_Bs when the radiometer is well within (far outside) the rain shaft. The difference is almost imperceptible at 10.7 GHz but can reach values as high as 15–20 K at 36.5 GHz.

[30] 6. There is an extended region outside the rain shaft with significantly positive *PD*s (larger than 2K) at 36.5 (and at 21.0 GHz, not shown). The 1D pencil beam cannot

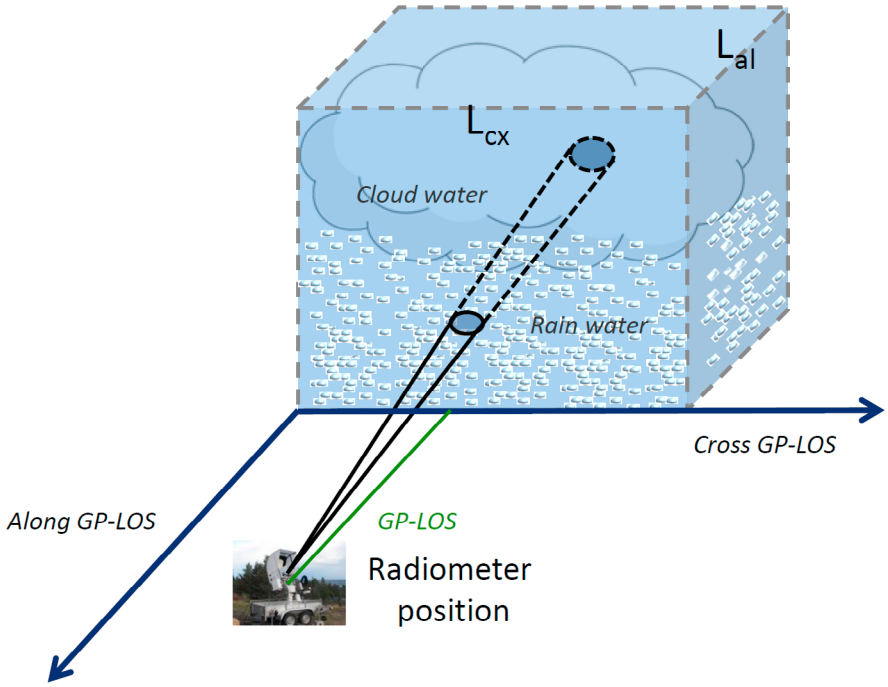

Figure 9. Schematic for the rain cloud simulation. Radiances have been computed at the radiometer location identified by the coordinate (Along *GP-LOS*, Cross *GP-LOS*). The blue shaded area contains the rain system which has a vertical but no horizontal structure. The length of the horizontal sides of the cloud box are L_{al} and L_{cx}. Nonshaded areas contain only atmospheric gases. The surface is assumed to be a blackbody.

reproduce this feature, and *PD*s are even slightly below zero in the same region in a 1D approximation. While at 10.7 GHz *PD*s are always negative and can also achieve extremely negative values when the radiometer is located either within or outside of the rain shaft (feature well depicted in Figure 6 and confirmed for the whole set of observations in Figure 2a), there is only a confined region at 36.5 GHz where large negative *PD*s are reached (Figure 10, bottom right). This situation is achieved when the radiometer is looking from underneath the rain shaft, having a small portion of the precipitating cell in the FOV (around one optical thickness). In that region, 3D simulations generally favor more negative *PD* values than 1D-SP.

better insight is provided by analyzing the contribution of the different orders of scattering to the signal. The zero order of scattering term (i.e., the emission term, red diamonds in Figure 11) is perfectly accounted for by a 1D-SP approximation. These differences must result from higher order of scattering terms. As visible in Figure 11 (right) the structure of the *PD* signal is driven by the first order of scattering. For scenarios involving horizontally oriented flattened raindrops the first order of scattering tends to produce negative *PD*s (blue squares). Hereafter we generalize the theoretical argument proposed by *Battaglia and Simmer* [2007, equations (17)–(21)]: at the surface ($z = 0$) the jth order of the downwelling T_B sensed at a given direction (μ_r, ϕ_r) is given by

$$\begin{pmatrix} T_V^{\downarrow[j]}(\mu_r,\phi_r) \\ T_H^{\downarrow[j]}(\mu_r,\phi_r) \end{pmatrix} = \begin{pmatrix} \int_{sl} e^{-\tau_{sl}^{\downarrow V}(\mu_r,\phi_r,z')} \overbrace{\int \left[Z_{vv}(\mu_i,\mu_r,\Delta\phi) T_V^{[j-1]}(\mu_i,\phi_i,z') + Z_{vh}(\mu_i,\mu_r,\Delta\phi) T_H^{[j-1]}(\mu_i,\phi_i,z') \right] d\Omega_i}^{\mathcal{J}_V^{[j-1]}(\mu_r,z')} \frac{dz'}{|\mu_r|} \\ \int_{sl} e^{-\tau_{sl}^{\downarrow H}(\mu_r,\phi_r,z')} \overbrace{\int \left[Z_{hv}(\mu_i,\mu_r,\Delta\phi) T_V^{[j-1]}(\mu_i,\phi_i,z') + Z_{hh}(\mu_i,\mu_r,\Delta\phi) T_H^{[j-1]}(\mu_i,\phi_i,z') \right] d\Omega_i}^{\mathcal{J}_H^{[j-1]}(\mu_r,z')} \frac{dz'}{|\mu_r|} \end{pmatrix}, \quad (1)$$

5. Discussion

5.1. Anisotropic Scattering Effects

[31] The three last observations described above deserve further discussion. What is the fundamental cause of the difference between 1D-SP and 3D radiative transfer? A

where Z is the ensemble-averaged phase matrix (whose elements are expressed in the H-V basis). The outer integral is performed over the slant volume and accounts for the propagation effect, i.e., the larger H extinction of the medium, which tends to produce V-polarized radiation (positive *PD*s). The inner integral accounts for the polarization effect of the

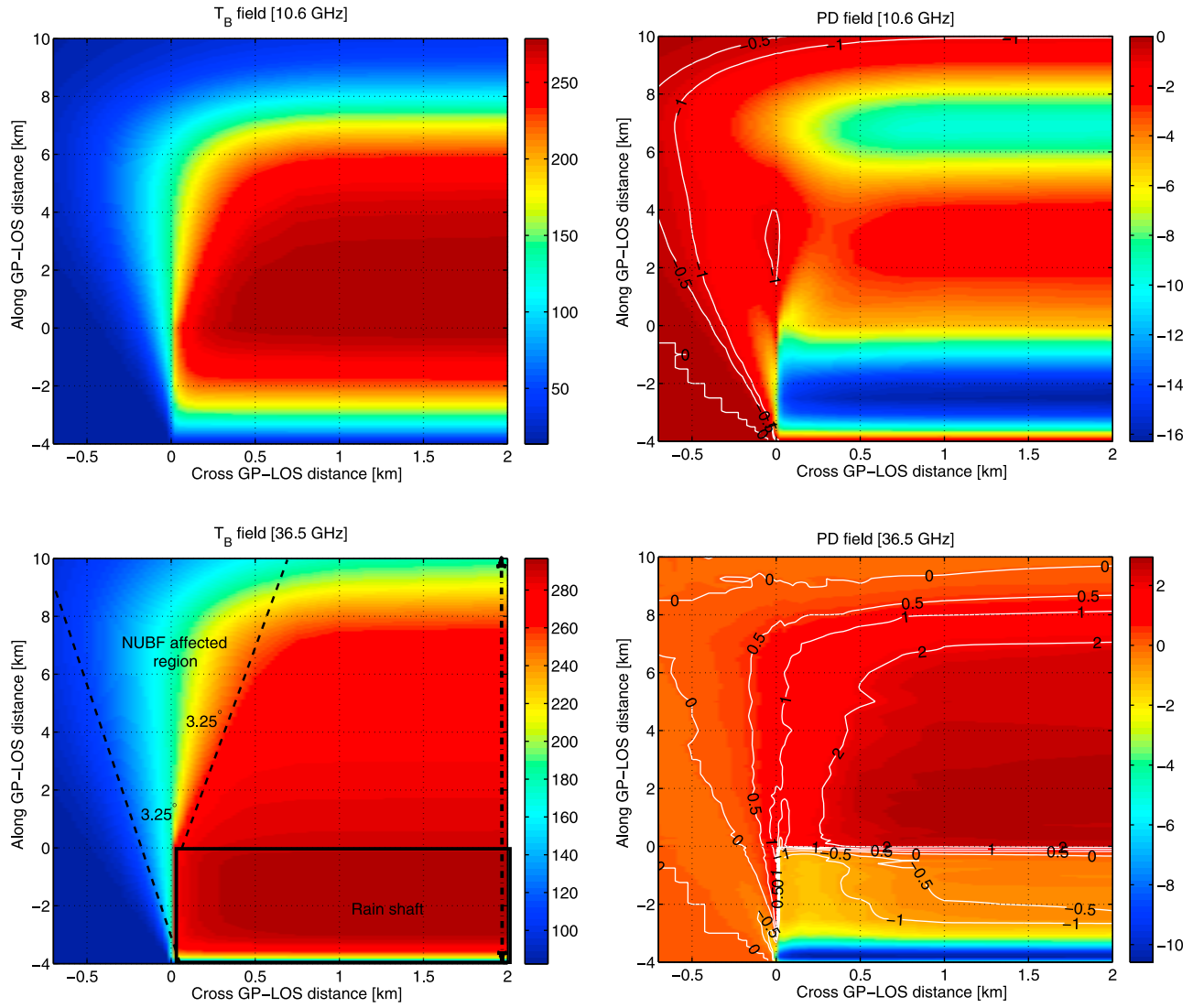

Figure 10. (left) Brightness temperatures and (right) polarization differences as sensed by an ADMIRARI-type radiometer looking "southward" (i.e., downward in the image) at an elevation angle of 30° for (top) 10.7 GHz and (bottom) 36.5 GHz. The different radiometer viewing positions are identified by two coordinates: the along- and cross-ground-projected line-of-sight (GP-LOS) distances.

scattering from all possible incoming directions (μ_i, ϕ_i) into the radiometer viewing direction (μ_r, ϕ_r). Note that with preferentially oriented azimuthally symmetric distributed hydrometeors the phase matrix depends only on the relative azimuth difference $\Delta\phi = \phi_i - \phi_r$. For the polarization difference at scattering order j we can write

$$PD^{[j]}(\mu_r, \phi_r) \propto \langle \mathcal{J}_V^{[j-1]} \rangle_{sl} - \langle \mathcal{J}_H^{[j-1]} \rangle_{sl}, \tag{2}$$

where the brackets indicate an averaging along the slant volume. Reverting to the linear basis [$T \equiv 0.5(T_V + T_H)$, $PD \equiv T_V - T_H$] the contribution of the first order of scattering to polarization will be

$$PD^{[1]}(\mu_r, \phi_r) \propto \langle \int \Big[2Z_{21}(\mu_i, \mu_r, \Delta\phi)\ T^{[0]}(\mu_i, \phi_i) + Z_{22}(\mu_i, \mu_r, \Delta\phi)\ PD^{[0]}(\mu_i, \phi_i) \Big]\ d\Omega_i \rangle. \tag{3}$$

In the specific CHUVA setup $\mu_r = -0.5$ and given the amplitude of $T^{[0]}$ and $PD^{[0]}$ and the behavior of Z_{21} and Z_{22} (not shown) the first term within the integral is dominant. Thus it is worthy to analyze the dependence of the phase matrix scattering element Z_{21} on the incoming direction ($\theta_{in} = a\cos(\mu_i)$) and the relative azimuth difference when $\mu_r = -0.5$. Figure 12 (left) depicts a typical behavior for Z_{21} at 36.5 GHz (but the same is found at the other ADMIRARI frequencies with large horizontally oriented raindrops). The azimuth dependence of the phase matrix elements is the result of two effects: (1) the dependence of the scattering angle on $\Delta\phi$ (with the related dependence of polarization on the scattering angle) and (2) the rotation needed to relate the Stokes parameters of the incident and scattered beams relative to their meridional planes (details in chapter 1 of *Mishchenko et al.* [2000]) which, for instance, accounts for the azimuthal dependence at $\theta_{in} = 0°$, 180° in Figure 12. Figure 12 (right) shows the same element azimuthally averaged, i.e., the phase

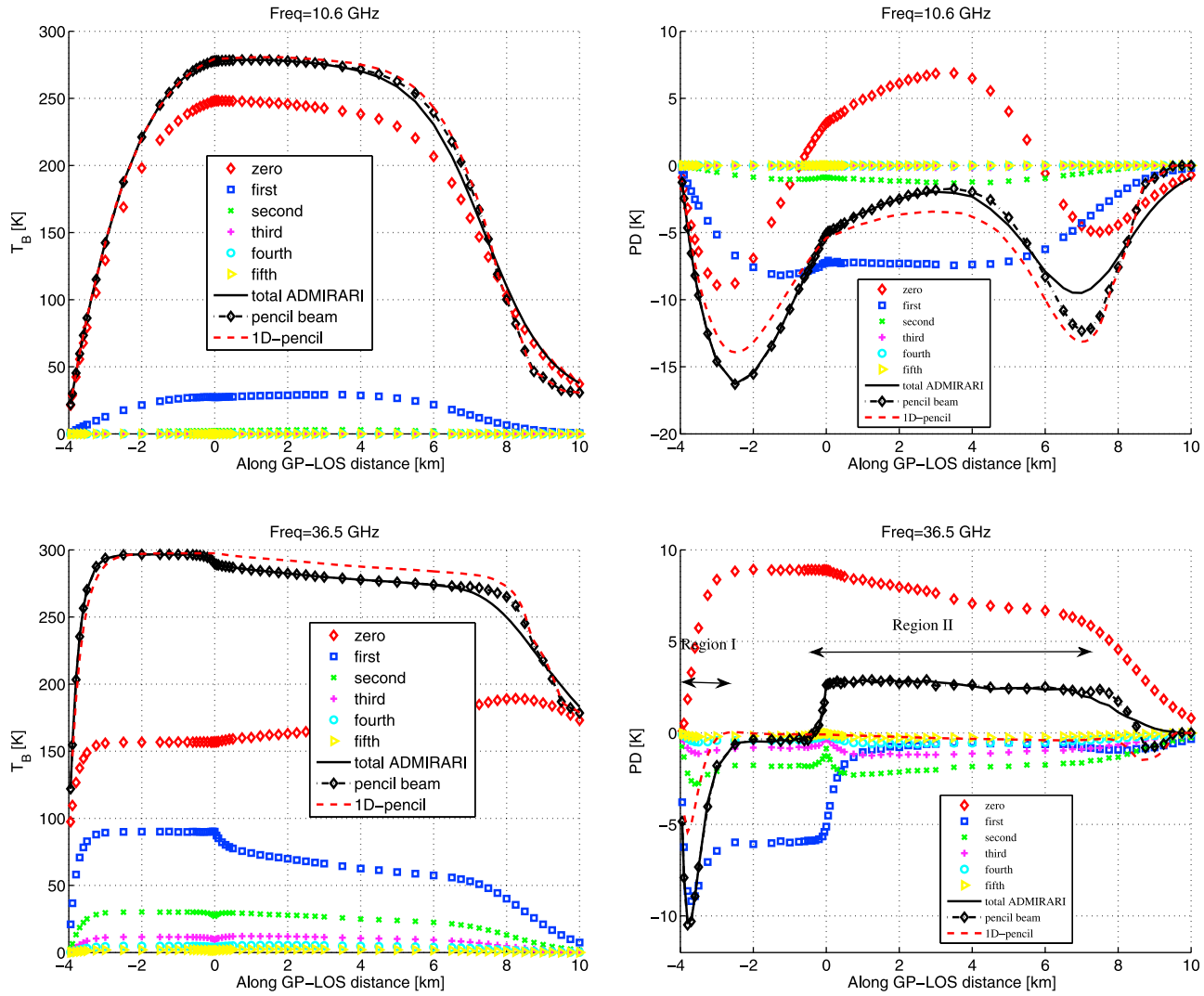

Figure 11. Contribution of different order of scattering (left) to the brightness temperatures and (right) to the polarization differences for different radiometer positions of Figure 10 along the line with a cross-ground-projected line-of-sight (GP-LOS) distance equal to 2 km (dash-dotted line in Figure 10, bottom left) for (top) 10.7 GHz and (bottom) 36.5 GHz.

matrix element used in a 1D approximation where there is no azimuth dependence of the radiation field.

[32] The major differences between 3D and 1D-SP are found when the radiometer is located immediately underneath the rain shaft and when the radiometer is outside of the rain shaft. The two situations are illustrated in Figure 13.

[33] The first configuration (Figure 13, top) is representative of region I (along-GP-LOS distance from the rain shaft between −4 and −3 km, i.e., inside the rain shaft in Figure 11). In this case the radiometer is only looking through rain (the cloud base is at 3 km) and, even at 36.5 GHz, the signal is not fully saturated. Very negative values for polarization are reached at 36.5 GHz in the 3D simulation. The 1D-SP approximation is producing lower T_Bs and higher *PD*s. The 1D RT is run on a 1D domain, which is derived by extending horizontally the domain intercepted by the slant ADMIRARI volume (Figure 13, red dash-dotted line rectangle). Therefore, while the radiation emitted within the slant volume is perfectly accounted for, the scattered radiation is not. Let us consider here the radiation sensed by the radiometer scattered once only, and within the ADMIRARI FOV. The 1D approximation introduces fictitious scattering events like those illustrated with the red dash-dotted arrows in Figure 13, i.e., corresponding to radiation emitted from outside the sides of the box and emitted downward (side leakages, positive contribution). Conversely, the 1D approximation is missing the radiation coming from the upper part of the box in Figure 13 (blue region), for example, the contributions illustrated with the blue dashed lines (leakages from the upper part of the rain shaft, negative contribution). Moreover, part of the radiation coming from the surface is scattered by the rain medium and therefore the first order of scattering component is penalized in favor of higher order of scattering radiation. Overall, in the 1D approximation, there will be also a loss and a reduction of the radiation traveling upward within the radiometer volume due to radiation escaping to space (negative leakages to space). In the 1D approximation the suppression of the upwelling $I^{[0]}$ coming

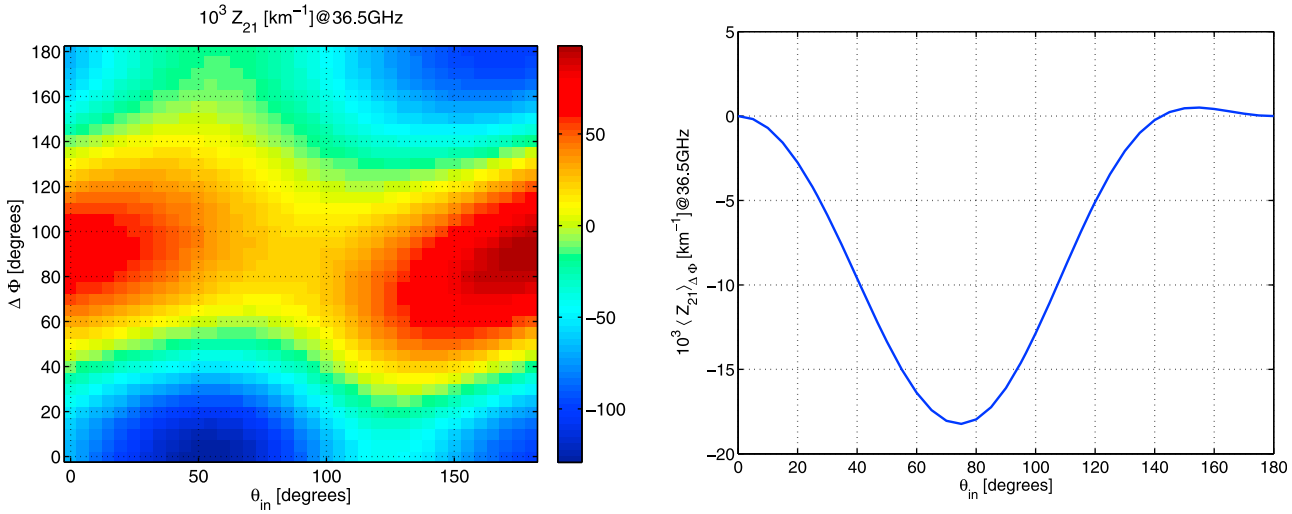

Figure 12. (left) Phase function element Z_{21} for θ_r = 150° for a Marshall and Palmer distributed rain layer with a rain content of 2.8 g/m^3. (right) Azimuthally averaged phase function element $\langle Z_{21} \rangle_{\Delta\Phi}$ from Figure 12 (left).

from the right side of the rain shaft represents the most relevant source for the reduction of the negative amplitude of the *PD* signal at small optical thickness. In the 3D RT, there is a surplus of radiation coming from angles θ_i between 0 and 90° which is scattered back to the radiometer with $\Delta\Phi$ around zero. For this range of angles, Z_{12} assumes strongly negative values (lower left corner in Figure 12, left), thus explaining the strongly negative *PD*s in the 3D computations. The leakages from the top have also a relevant effect since they relate to Z_{12} values with θ_i close to 180° but with predominant $\Delta\Phi$ values around 180°. To summarize, in the 1D approximation the positive leakages from the side are smaller than the negative leakages from the top and to space. The overall effect is to reduce T_Bs. In addition to that, the 1D approximation tends to favor a radiation field within the radiometer volume characterized by larger orders of scattering; since radiation scattered many times tends to be unpolarized this also explains the less negative *PD*s in region I.

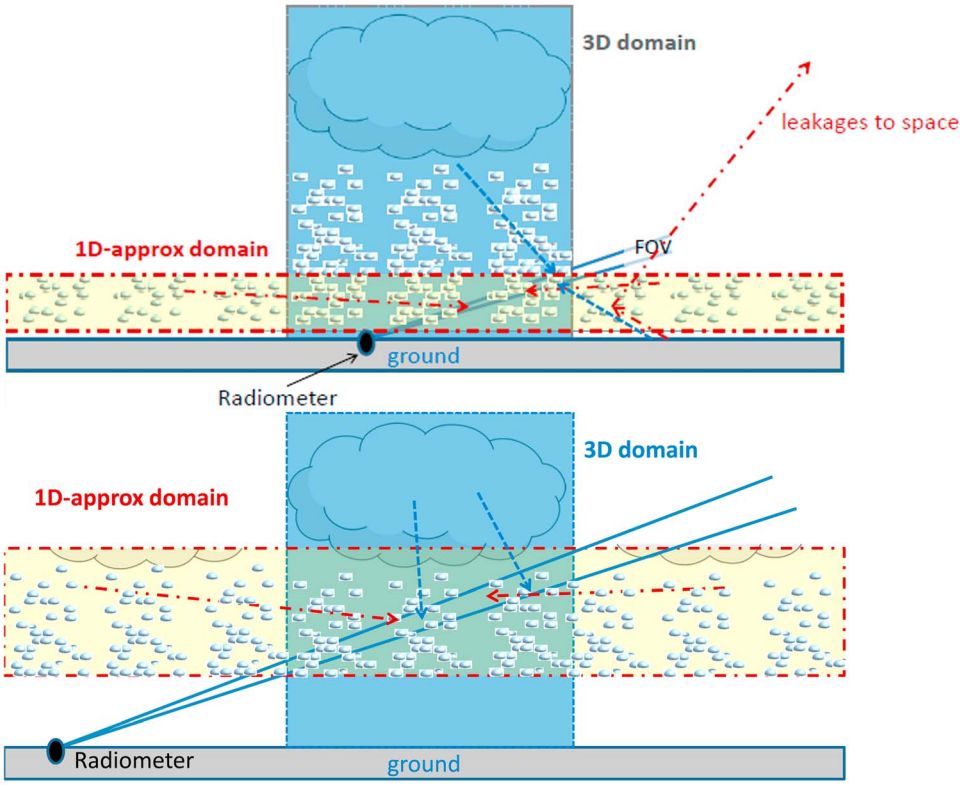

Figure 13. Schematic for understanding 3D effects when the radiometer is (top) underneath the rain shaft and (bottom) outside of it.

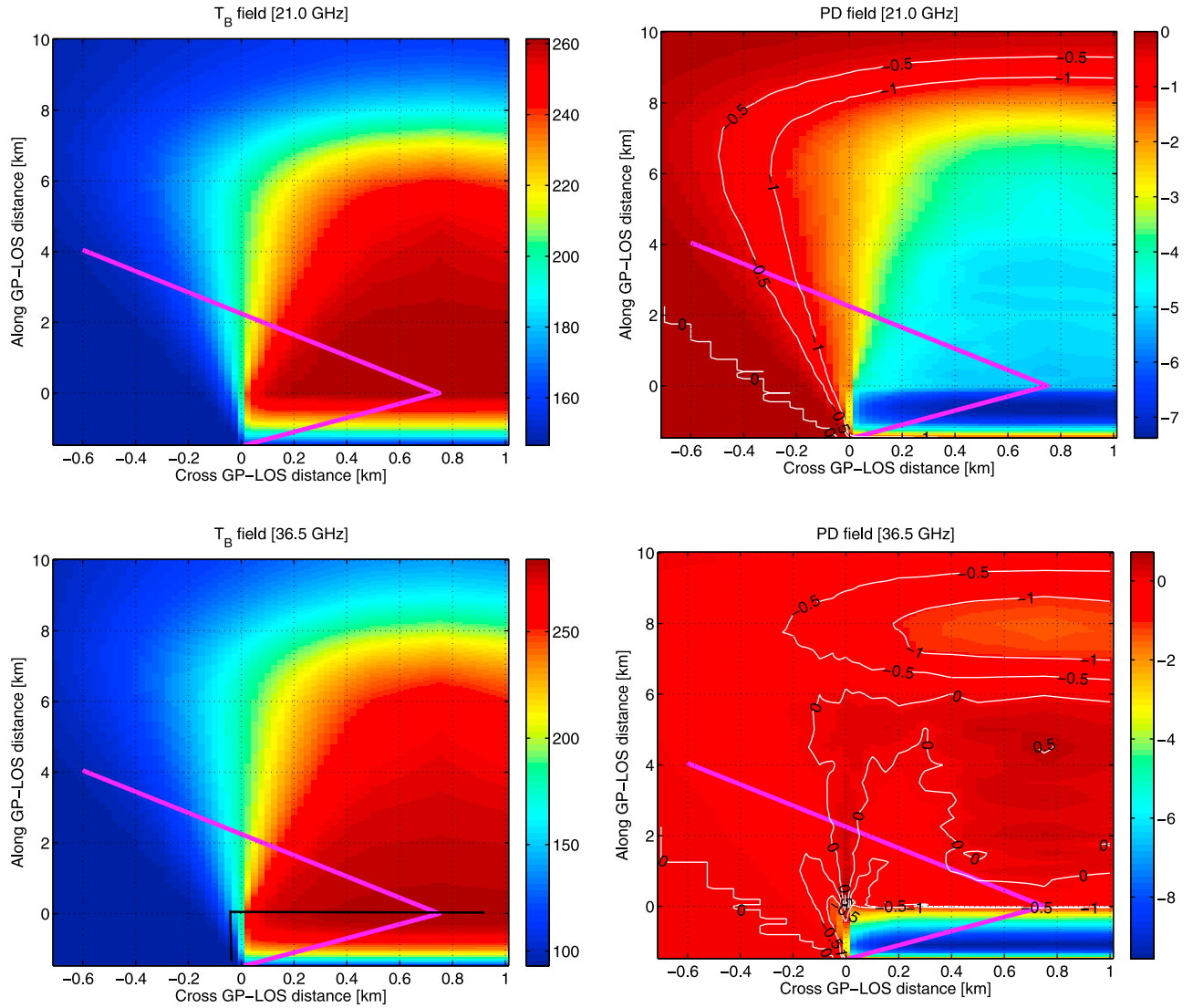

Figure 14. Same as in Figure 10 but for the (top) 21 and (bottom) 36.5 GHz channels and for a scenario more appropriate for the 19 March event: L_{cx} = 1.5 km and L_{al} = 1.5 km. The magenta line is a guessed position of the radiometer during the 19 March event.

[34] Conversely, when the radiometer is in the region II (along-GP-LOS distance from the rain shaft between −0.5 and 8 km in Figure 11) the leakages from the side play the most important role. In fact the signal is now close to saturation and the volume effectively contributing to the radiometer signal is confined to a region at most few hundred of meters within the rain shaft (so the leakages from the top have no relevance at all). The situation is reversed from the former case with the 1D approximation T_Bs exceeding the ones computed accounting for the full 3D structure. The radiation corresponding to these side leakages is generally characterized by incoming polar angle θ_{in} slightly above 90° and by $\Delta\Phi$ around 180°. The scattering phase function for those angles is significantly negative (center upper part in Figure 12, left). The absence of such radiation in the real 3D world does produce the positive *PD*s we actually observe. In a 1D-SP RT on the other hand all the profiles having along-GP-LOS distances from the rain shaft in the range [−2.5, 8] km look quite similar and tend to have T_Bs approaching the ones characteristic of a blackbody, thus unpolarized.

[35] In summary, there is an azimuthal anisotropy of the radiation field within the radiometer FOV when looking at a rain shaft from outside at slant angles. This anisotropy, in combination with the peculiar structure of the phase function elements of preferentially horizontally oriented raindrops (Z_{21} is predominantly negative when azimuthally averaged), produces the puzzling positive *PD*s, which are ubiquitous in our CHUVA observations. On the other hand, in a 1D approximation the radiation field has no azimuthal dependence, modifications of the radiation fields caused by horizontal variability cannot be accounted for, and the observed positive *PD*s cannot be reproduced in a simulation framework because of the behavior of $\langle Z_{21} \rangle_{\Delta\Phi}$. The simultaneous collocated observations tend to exclude other possible explanations of the phenomenon of positive *PD*s observed at 36.5 GHz. For instance, a huge amount of

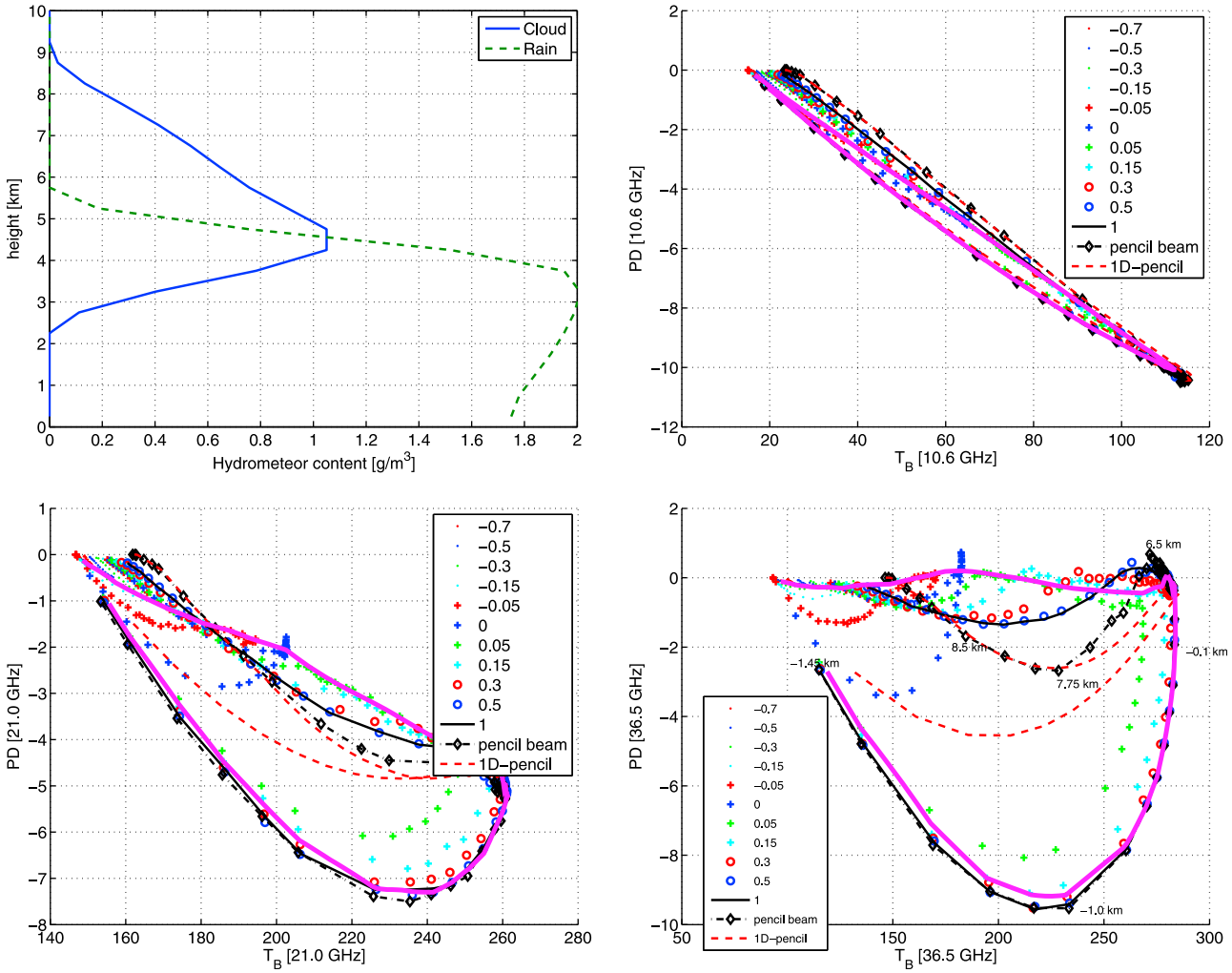

Figure 15. (top left) Hydrometeor profile considered to match the case observed on 19 March 2010. (top right and bottom) The spatial evolution in the $T_B - PD$ space is shown when moving from within to the outside of the rain shaft for different cross-GP-LOS distances as indicated in the legend. Each line is traveled counterclockwise. The magenta line corresponds to simulated observations in correspondence to the magenta path shown in Figure 14.

cloud water located beyond a small amount of horizontally oriented raindrops could potentially produce positive polarization at 35 GHz via differential extinction but such scenario is excluded by the simultaneous large negative *PD*s at 10.6 GHz and by the high MRR reflectivities.

5.2. NUBF Effects

[36] An additional complication is added when NUBF situations are present. Let us reconsider the time evolution shown in Figure 5. Again we resort to a simple square rain shaft with sides equal $L_{al} = 1.5$ km and $L_{cx} = 2$ km similar to that observed at 2048 UTC according to the RHI profile (Figure 4, top right) and to the MRR reflectivity (Figure 3a) to interpret the measurements. Similarly to Figure 10, simulated T_Bs and *PD*s for the 21 and 36.5 GHz channels are shown in Figure 14. The vertical hydrometeor profile here assumed is plotted in Figure 15 (top left). Figure 15 (top right and bottom) depicts the change in the $T_B - PD$ plane when moving the radiometer observation point along the radiometer viewing direction with an along-GP-LOS distance from the rain shaft from −1.45 km to 10 km, i.e., passing from inside to outside the rain along the line of sight. Different lines correspond to different positions relative to the rain shaft border in the direction orthogonal to the radiometer line of sight, as indicated by the legend. When considering radiometer locations distant from the rain shaft edge (i.e., those labeled with a cross-GP-LOS distance equal to 1 km) the counterclockwise transition from the point with along-GP-LOS distance from the rain shaft equal to −1.45 km to that with along-GP-LOS distance equal 8 km can be interpreted as if a cell with stationary rain has passed over the radiometer and has moved away along the line of sight of the radiometer. Such patterns (black lines in Figure 15) qualitatively resemble the temporal evolution of $T_B - PD$s measured at the three frequencies (Figure 5). At 36.5 GHz, there is a "spatial accumulation point" for T_B ~280 K and *PD* ~0; that is, there is no spatial variability in the simulated signal for observation points located from the rain shaft edge up to an along-GP-LOS distance from the rain shaft of about 6 km. At such far distance the radiometer

starts sensing the decrease in rain content at around 4 km altitude and the presence of cloud droplets as well (Figure 15, top left). Similarly, in Figure 5, there is a "temporal accumulation point," with measurements dwelling at the same location in the 36.5 GHz $T_B - PD$ plane between 2045 and 2047 UTC at $T_B \sim 270$ K. Assuming that the storm is moving at 8 m/s, this will produce a movement of 1.5 km in 3 min (and of 4 km for the whole duration of the event), which is inconsistent with the former length estimate (4 times larger). It is therefore very likely that the storm did not move along the line of sight of the radiometer but on the other hand crossed its FOV. This is in agreement with the two consecutive PPI images of Figure 4 which suggest movement of the rain cells from the east to west. In this case, in Figure 15, instead of dwelling on the continuous black line, the measurements would have progressively jumped on the other symbol lines (circle, then crosses, then dots), undergoing a strong T_B gradient. This actually also better explains the presence of near-null *PD*s in the 36.5 GHz channel for T_Bs below 250 K. The accumulation of measurements in such region of the $T_B - PD$ plane is likely to be the result of NUBF effects and to occur when precipitating systems are migrating out of the radiometer FOV.

[37] To verify our assumption, according to our auxiliary observations for the 19 March event, a sequence of positions of ADMIRARI relative to our simulated rain shaft has been assumed (magenta line in Figure 14, bottom). Note that the sharp change of direction is a pure graphical artefact; the problem is indeed symmetric respect to the vertical line where cross-GP-LOS is equal to 0.75 km. The radiometer is first under the rain shaft, and then the rain cell is moving away from the radiometer and exiting its FOV, which is consistent with the MRR observation (Figure 3a), rain shaft going away from the radiometer) and with the PPI image (Figure 4, cell crossing the FOV from east to west). The magenta lines in Figure 15 correspond to this possible solution; these three patterns resemble the ones observed in Figure 5 with all the limitations of the case.

[38] It is important to note that in the 10.7 GHz channel the along line of sight optical thicknesses of precipitating media are generally small, *PD*s are linearly decreasing with T_Bs, so that, in the $T_B - PD$ plane, points corresponding to NUBF scenes fall in the same region of uniform beam filled (UBF) scenes (Figure 15, top right) and the structure of the $T_B - PD$ curve does not suffer significant changes. Because of the nonlinearities between the radiometer signal and the retrieved quantities (cloud and rain integrated water path) such ambiguities introduce additional uncertainties in the retrieval. In addition to that, at 21.0 and 36.5 GHz the pronounced concave upward behavior of the $T_B - PD$ curves permits the exploration of new regions in the $T_B - PD$ plane uncovered by UBF scenes (e.g., blue crosses in Figure 15, bottom right). The inclusion of NUBF effects is therefore mandatory to cover the full range of observations in the *PD*s space and to decrease the residuals in any Bayesian-type retrieval.

6. Conclusions

[39] The CHUVA GPM/GV campaign has been a unique opportunity in understanding 3D effects related to microwave ground-based polarimetric observations of rain systems. During CHUVA, many events were observed by ADMIRARI, all of them characterized by an overwhelming 3D structure with small localized rain elements surrounded by clear air. The occurrence of warm rain events and the simultaneous acquisitions of collocated X band RHI scans greatly facilitated the RT interpretation. By investigating some case studies, we can draw the following conclusions for polarimetric ground-based radiometer observations.

[40] 1. Geometric 3D effects are, obviously, always affecting measurements performed at slant angles. They can be easily accounted for by adopting 1D slant path approximations.

[41] 2. In heavy rain, for radiometers with frequencies in the 10–36 GHz region, the scattered component represents a large fraction (increasing with frequency) of the total signal; for instance, at 36 GHz, raindrops are both absorbing and scattering microwave radiation with single scattering albedos easily exceeding 0.5. The overall power detected by the radiometer is therefore the result both of emission and of scattering processes within the FOV of the radiometer, and 3D scattering effects are likely to occur.

[42] 3. The *PD* signal is particularly sensitive to scattered radiation with the first order of scattering contributing crucially to the overall signal. The polarization property of the scattered radiation is driven by the Z_{12} phase matrix element of the scattering medium along the radiometer line of sight. For perfectly oriented spheroids like raindrops and for radiometer observations at 30° elevation angle, this term can assume both positive and negative values, depending on the relative geometry of the incoming/outgoing radiation, with a strong dependence on the relative azimuth. Radiation fields with strong azimuthal inhomogeneities (like those produced by side leakages) can produce large departures from the polarization signals produced when adopting 1D SP approximations (which inherently assume azimuthal symmetric radiation fields).

[43] 4. Observations of *PD*s as high as +4 K and +2.5 K at 36.5 GHz and 21.0 GHz, respectively, in combination with almost saturated T_B s are clear 3D scattering fingerprints. As a consequence, the interpretation of *PD* signals for the 21 and 36.5 GHz channels is utterly difficult at large optical thicknesses because they are heavily influenced by the 3D structure of the system. This poses serious problems when interpreting the *PD* results for instance in the implementation of ADMIRARI-like physically based schemes tailored to retrieve integrated cloud and rain water paths.

[44] 5. Due to the smaller footprint, ground-based observations are potentially less affected by NUBF than spaceborne observations and therefore more suited for pristine studies of the radiation field. However, when the precipitating system is tall (e.g., in tropical environments) and it is located far away from the radiometer position, NUBF can play a relevant role as well. Because of the nonlinear response of *PD*s with T_Bs and of both these quantities with the variables to be retrieved (cloud and rain integrated water path), NUBF is difficult to disentangle. Its effect is twofold: either it bears ambiguities (i.e., measurements with the same *PD*s and T_Bs but corresponding to different microphysical states) or it favors the occurrence of *PD*s and T_B unpredicted by UBF scenarios.

[45] The current analysis stresses thorny issues related to 3D RT effects present in physically based schemes aimed at retrieving integrated cloud and rain water paths from

ADMIRARI-like observations. The introduction of highly resolved (500 m resolution or less) cloud model runs (tailored to the different synoptic conditions experienced during the measurement field campaigns) coupled with full 3D RT models represents the most rigorous modus operandi for the foundation of a RT database suited for a Bayesian retrieval scheme. This is the strategy we are currently pursuing for an optimal interpretation of ADMIRARI observations.

[46] **Acknowledgments.** The authors would like to thank the NASA GPM/GV program for funding the participation of ADMIRARI in the CHUVA campaign, the Brazilian GPM/GV counterpart for logistic assistance and cooperation during the experiment, and the access to auxiliary data. We are also grateful to C. Kummerow for useful discussions during the field campaign and afterward and to the reviewers for their comments. The ADMIRARI project has been funded by the Deutsche Forschungsgemeinshaft (DFG) under grant BA 3485/1-1. The authors are grateful for the financial support provided by the Brazilian Space Agency-AEB during the CHUVA field campaign at Alcantara, Brazil. One of the authors (C.A. Morales) was also partially supported by FAPESP grant 2009/15235-8 and Coordenação de Aperfeiçoamento de Pessoal de Nível Superior-CAPES. A. Battaglia was funded for his travels by the NCEO Mission Support funding.

References

Andsager, K., K. V. Beard, and N. S. Laird (1999), A laboratory study of oscillations and axis ratios for large raindrops, *J. Atmos. Sci.*, *56*, 2673–2683.

Battaglia, A., and S. Mantovani (2005), Forward Monte Carlo computations of fully polarized microwave radiation in non-isotropic media, *J. Quant. Spectrosc. Radiat. Transfer*, *95*(3), 285–308.

Battaglia, A. and C. Simmer (2007), Explaining the polarization signal from rain dichroic media, *J. Quant. Spectrosc. Radiat. Transfer*, *105*(1), 84–101, doi:10.1016/j.jqsrt.2006.11.012.

Battaglia, A., F. Prodi, F. Porcu, and D.-B. Shin (2005), 3D effects in MW radiative transport inside precipitating clouds: Modeling and applications, in *Measuring Precipitation From Space: EURAINSAT and the Future*, edited by V. Levizzani, P. Bauer, and F. J. Turk, pp. 113–126, Kluwer Acad., Norwell, Mass.

Battaglia, A., H. Czekala, and C. Simmer (2006), Three-dimensional effects in polarization signatures as observed from precipitating clouds by low frequency ground-based microwave radiometers, *Atmos. Chem. Phys.*, 4383–4394.

Battaglia, A., C. Davis, C. Emde, and C. Simmer (2007), Microwave radiative transfer intercomparison study for 3-D dichroic media, *J. Quant. Spectrosc. Radiat. Transfer*, *105*(1), 55–67, doi:10.1016/j.jqsrt.2006.09.017.

Battaglia, A., P. Saavedra, T. Rose, and C. Simmer (2009), Rain observations by a multi-frequency dual polarized radiometer, *IEEE Geosci. Remote Sens. Lett.*, *6*(2), 354–358.

Battaglia, A., P. Saavedra, T. Rose, and C. Simmer (2010), Characterization of precipitating clouds by ground-based measurements with the triple-frequency polarized microwave radiometer ADMIRARI, *J. Appl. Meteorol. Climatol.*, *49*, 394-414, doi:10.1175/2009JAMC2340.1.

Bauer, P., L. Schanz, and L. Roberti (1998), Correction of three-dimensional effects for passive microwave remote sensing of convective clouds, *J. Appl. Meteorol.*, *37*, 1619–1632.

Czekala, H. (1998), Effects of ice particle shape and orientation on polarized microwave radiation for off-nadir problems, *Geophys. Res. Lett.*, *25*(10), 1669–1672, doi:10.1029/98GL51132.

Czekala, H., and C. Simmer (1998), Microwave radiative transfer with nonspherical precipitating hydrometeors, *J. Quant. Spectrosc. Radiat. Transfer*, *60*(3), 365–374.

Czekala, H., S. Crewell, A. Hornbostel, A. Schroth, C. Simmer, and A. Thiele (2001a), Interpretation of polarization features in ground-based microwave observations as caused by horizontally aligned oblate rain drops, *J. Appl. Meteorol.*, *40*, 1918–1932.

Czekala, H., S. Crewell, C. Simmer, and A. Thiele (2001b), Discrimination of cloud and rain liquid water path by groundbased polarized microwave radiometry, *Geophys. Res. Lett.*, *28*(2), 267–270, doi:10.1029/2000GL012247.

Davis, C. P., C. Emde, and R. S. Harwood (2005), A 3D polarized reversed Monte Carlo radiative transfer model for mm and sub-mm passive remote sensing in cloudy atmospheres, *IEEE Trans. Geosci. Remote Sens.*, *43*, 1096–1101.

Davis, C. P., K. F. Evans, S. A. Buehler, D. L. Wu, and H. C. Pumphrey (2007), 3-D polarised simulations of space-borne passive mm/sub-mm midlatitude cirrus observations: A case study, *Atmos. Chem. Phys.*, *7*, 4149–4158.

Evans, K. F., and G. L. Stephens (1991), A new polarized atmospheric radiative transfer model, *J. Quant. Spectrosc. Radiat. Transfer*, *46*(5), 413–423.

Kummerow, C. (1998), Beamfilling errors in passive microwave rainfall retrievals, *J. Appl. Meteorol.*, *37*, 356–370.

Lafont, D., and B. Guillimet (2004), Subpixel fractional cloud cover and inhomogenety effects in microwave beam filling error, *Atmos. Res.*, *72*, 149–168.

Liu, Q., and C. Simmer (1996), Polarization and intensity in microwave radiative transfer, *Beitr. Phys. Atmos.*, *69*, 535–545.

Liu, Q., C. Simmer, and E. Ruprecht (1996), Three-dimensional radiative transfer effects of clouds in the microwave spectral range, *J. Geophys. Res.*, *101*(D2), 4289–4298, doi:10.1029/95JD03421.

Marshak, A., and A. B. Davis (Eds.) (2005), 3*D Radiative Transfer in Cloudy Atmospheres*, Springer, New York.

Mishchenko, M. I., J. W. Hovenier, and L. D. Travis (Eds.) (2000), *Light Scattering by Nonspherical Particles*, 690 pp., Academic, San Diego, Calif.

Mishchenko, M., et al. (2007), Accurate monitoring of terrestrial aerosols and total solar irradiance: Introducing the Glory mission, *Bull. Am. Meteorol. Soc.*, *88*, 677–691, doi:10.1175/BAMS-88-5-677.

Peters, G., B. Fischer, and T. Andersson (2002), Rain observations with a vertically looking Micro Rain Radar (MRR), *Bor. Environ. Res.*, *7*(4), 353–362.

Roberti, L., and C. Kummerow (1999), Monte Carlo calculations of polarized microwave radiation emerging from cloud structures, *J. Geophys. Res.*, *104*(D2), 2093–2104, doi:10.1029/1998JD200038.

Roberti, L., J. Haferman, and C. Kummerow (1994), Microwave radiative transfer through horizontally inhomogeneous precipitating clouds, *J. Geophys. Res.*, *99*(D8), 16,707–16,716, doi:10.1029/94JD01150.

Weinman, J. A., and R. Davies (1978), Thermal microwave radiances from horizontally finite clouds of hydrometeors, *J. Geophys. Res.*, *83*(C6), 3099–3107, doi:10.1029/JC083iC06p03099.

A. Battaglia, Department of Physics and Astronomy, University of Leicester, University Road, LE1 7RH Leicester, UK. (a.battaglia@le.ac.uk)

C. A. Morales, Instituto de Astronomia, Geofisica e Ciéncias Atmosféricas, Universidade de São Paulo, Rua do Matão, 1226, São Paulo, Brazil. (morales@model.iag.usp.br)

P. Saavedra and C. Simmer, Meteorological Institute, University of Bonn, Auf dem Hügel 20, D-53121 Bonn, Germany. (pablosaa@uni-bonn.de; csimmer@uni-bonn.de)